

Integration of Thermoelectric Generator and Wireless Sensor Node Simulators

M3CA-14-ID-BSU_-0704-0111

Vivek Agarwal
Yanliang Zhang

September 2016



The INL is a U.S. Department of Energy National Laboratory
operated by Battelle Energy Alliance

DISCLAIMER

This information was prepared as an account of work sponsored by an agency of the U.S. Government. Neither the U.S. Government nor any agency thereof, nor any of their employees, makes any warranty, expressed or implied, or assumes any legal liability or responsibility for the accuracy, completeness, or usefulness, of any information, apparatus, product, or process disclosed, or represents that its use would not infringe privately owned rights. References herein to any specific commercial product, process, or service by trade name, trade mark, manufacturer, or otherwise, does not necessarily constitute or imply its endorsement, recommendation, or favoring by the U.S. Government or any agency thereof. The views and opinions of authors expressed herein do not necessarily state or reflect those of the U.S. Government or any agency thereof.

Integration of Thermoelectric Generator and Wireless Sensor Node Simulators

Vivek Agarwal¹
Yanliang Zhang²

September 2016

¹Idaho National Laboratory
Idaho Falls, Idaho 83415
<http://www.inl.gov>

²Boise State University
Boise, Idaho 83725

Prepared for the
U.S. Department of Energy
Office of Nuclear Energy
Under DOE Idaho Operations Office
Contract DE-NE0008255

ABSTRACT

Collaborative research among Idaho National Laboratory, Boise State University, and the University of Houston under the Nuclear Energy Enabling Technologies Program's Advanced Sensors and Instrumentation Pathway aims to develop efficient and reliable thermoelectric generators (TEGs) for self-powered wireless sensor nodes (WSNs) for nuclear applications. The power harvesting technology has crosscutting significance to all U.S. Department of Energy Office of Nuclear Energy research and development programs, because the technology will enable self-powered WSNs in multiple nuclear reactor designs and spent fuel storage facilities using thermal energy available in a nuclear power plant or spent fuel storage facility. This project will address the technology gap that exists in realizing truly wireless sensor nodes due to the need for cables to connect to external power supplies and develop thermoelectric (TE) power harvesting devices to deliver sufficient power to drive the WSNs. The outcomes of the project will lead to significant advancement in sensors and instrumentation technology, reducing cost, improving monitoring reliability, and therefore enhancing safety. The self-powered WSNs could support the long-term safe and economical operation of all reactor designs and fuel cycle concepts, as well as spent fuel storage and many other nuclear science and engineering applications.

Most wireless sensor network (comprising thousands of WSNs) applications require operation over extended periods of time beginning with their deployment. Network lifetime is extremely critical for most applications and is one of the limiting factors for energy-constrained networks. Based on the application, there are a wide range of different energy sources suitable for powering WSNs. A battery is traditionally used to power WSNs. The deployed WSN is required to last for a long time. Due to the finite amount of energy present in batteries, it is not feasible to replace batteries. Recently there has been a new surge in the area of energy harvesting where ambient energy in the environment can be utilized to prolong the lifetime of WSNs. Some of the sources of ambient energies are solar power, thermal gradient, human motion and body heat, vibrations, and ambient radio frequency energy.

This report focuses on integrating TEG and WSN simulators with a direct-current-to-direct-current (DC-DC) converter as an interface. A DC-DC converter is essential to balance a wide range of analog, digital, and radio loads acting on the energy source. Also, the voltage level generated by TEGs under varying temperature conditions could be low, irregular, and insufficient to operate a WSN; therefore, DC-DC is required to boost the voltage to a desired level. Most of the main problems with DC-DC converters used in a TEG system are related to impedance matching between the internal resistance of the TEG and the input resistance of the DC-DC converter. This report addresses the issue associated with dynamic impedance matching under varying temperature conditions in the effort to integrate TEGs and WSNs.

In this effort, dynamic impedance matching algorithms like perturb and observe and extremum-seeking control algorithms will be implemented and compared to achieve maximum peak power tracking. In addition, the report will summarize the study performed at Boise State University on profiling behavior of WSN prototype.

ACKNOWLEDGMENTS

This report was made possible through funding by the U.S. Department of Energy's Nuclear Energy Enabling Technologies Program. We are grateful to Suibel Schuppner at the U.S. Department of Energy and Bruce Hallbert at Idaho National Laboratory for championing this effort. We thank Jodi L. Vollmer and Jim Nelson for technical editing and formatting the document.

CONTENTS

ABSTRACT	iii
ACKNOWLEDGMENTS	v
ACRONYMS	xi
1. INTRODUCTION.....	1
1.1 Project Background	1
1.2 Problem Statement.....	1
1.3 Report Layout.....	2
2. MODELING	3
2.1 Thermoelectric Modeling Overview.....	3
2.1.1 Thermoelectric Model.....	3
2.1.2 Heat Sink Model.....	5
2.1.3 Combined Heat Transfer Model.....	6
2.1.4 Heat Sink Optimization.....	7
2.1.5 Thermoelectric Generator Optimization	8
2.1.6 Thermoelectric Module Results	8
2.2 Wireless Sensor Node Modeling	10
3. DC-DC CONVERTERS	11
4. THERMOELECTRIC GENERATION AND WIRELESS SENSOR NODE INTEGRATOR.....	13
4.1 Maximum Peak Power Tracking	13
4.2 Perturb and Observe Algorithm.....	13
4.3 Extremum Seeking Control Algorithm.....	15
4.4 Implementation of Maximum Peak Power Tracking Algorithms and Results.....	17
5. EXPERIMENTAL DATA ON WIRELESS SENSOR NODE	19
6. CONCLUSIONS AND FUTURE WORK	21
7. REFERENCES.....	23
Appendix A Numerical Analysis of Maximum Peak Power with Extremum-Seeking Control	26

FIGURES

Figure 1. Schematic of self-powered WSN using TEG.....	1
Figure 2. Input power of a DC-DC converter as a function of its input resistance.....	2
Figure 3. Heat transfer model accounting for the heat flow through the TEG and the heat sink, where Q_H is the heat flow into the hot side of the TEG, Q_C is the heat leaving the cold side of the TEG, and Q_{HS} is the heat flow from the heat sink to the ambient side. The heat sink plates are vertically oriented; the figure illustrates a top view.	3
Figure 4. Temperature-dependent properties of the Half-Heusler p-leg and n-leg: (a) Seebeck coefficient, (b) electrical resistivity, and (c) thermal conductivity.	5
Figure 5.(a) Thermal insulant for varied fin heights and fin thicknesses, (b) minimum thermal insulant for varied fin thicknesses for a plate height of 20 cm, (c) thermal insulant for varied packing fractions for a fin thickness of 2 mm and fin height of 20 cm.	7
Figure 6. TE power density for varied TE leg heights from 1 mm to 1.8 mm for a leg packing fraction of 15.75%.	8
Figure 7. (a) TEG power output for varied load resistances that produce distinct currents at hot-side temperatures of 420°C, 320°C, and 220°C and an ambient temperature of 20°C. (b) TEG voltage as a function of current for varied load resistances at hot-side temperatures of 420°C, 320°C, and 220°C and an ambient temperature of 20°C.	9
Figure 8. (a) Hot-side temperature variation with time and peak TEG power obtained when the respective hot-side temperature is used with an ambient temperature of 20°C. (b) Corresponding TEG voltage and current required for peak power in Figure (a).	9
Figure 9. State transition diagram (Agarwal 2011).	11
Figure 10. Circuit diagrams for the buck (a), boost (b), and buck-boost (c) converters (Jahanbakhsh 2012, Kotak and Tyagi 2013).	12
Figure 11. Simplified circuit diagram of an isolating DC-DC buck converter (Li 2011).	12
Figure 12. Schematic illustration of MPPT in a TEG-powered WSN.	13
Figure 13. Flow chart of the P&O MPPT algorithm.	14
Figure 14. Illustration of oscillation in the P&O algorithm.	15
Figure 15. A block diagram of an ESC control system.	15
Figure 16. Illustrative cases of an ESC mechanism (Leyva et al. 2006).	16
Figure 17. MPP estimated using P&O algorithms at different hot-side temperatures.	17
Figure 18. Block diagram of a sine wave dithered ESC algorithm.	18
Figure 19. Response time and voltage measured across a micro-controller.	19
Figure 20. Response time and voltage measured across a microSD storage device.	19
Figure 21. Response time and voltage measured across a transceiver based on IEEE 802.15.4 communication protocol.	20
Figure 22. Response time and voltage measured across an assembled WSN.	20
Figure 23. Response of a WSN recorded as it transitions through different operational states defined in the state space S.	21

TABLES

Table 1. Optimized heat sink parameters.....	7
Table 2. Optimized TE module parameters.....	8
Table 3. Transfer function of different converter topology.....	12
Table 4. ESC parameter values.....	18
Table 5. Comparison of estimated MPP using P&O and ESC algorithms.....	18

ACRONYMS

BSU	Boise State University
DC	direct current
ESC	extremum seeking control
IEEE	Institute of Electrical and Electronics Engineers
INL	Idaho National Laboratory
MPP	maximum peak power
MPPT	maximum peak power tracking
P&O	perturb and observe
TE	thermoelectric
TEG	thermoelectric generator
WSN	wireless sensor node

Integration of Thermoelectric Generator and Wireless Sensor Node Simulators

1. INTRODUCTION

1.1 Project Background

The application of power harvesting technology to energize wireless sensor nodes (WSNs) has crosscutting significance to all U.S. Department of Energy Office of Nuclear Energy research and development programs, because the technology will enable self-powered WSNs (ORNL 2006) in multiple nuclear reactor designs and spent fuel storage facilities. Wireless communications enable the elimination of communication wires; a technology gap still exists in realizing truly WSNs due to the need for external power supply cables.

The Advanced Sensors and Instrumentation Pathway under the Nuclear Energy Enabling Technologies Crosscutting Technology Development Program is supporting this research project to address this important technology gap and develop thermoelectric (TE) power harvesting devices to deliver sufficient power to drive the WSNs. Advancements in TE material efficiency over the past decade (Mehta et al. 2012; Yan et al. 2012; Poudel et al. 2008) has sparked a great deal of research in this field when compared to other applications of power harvesting technologies. With the abundance of waste heat energy available in a nuclear facility, thermoelectric generators (TEGs) are one of the most promising power harvesting technologies that would benefit the nuclear industry. A collaborative team of researchers from Idaho National Laboratory (INL), Boise State University (BSU), and the University of Houston is performing this project. This partnership brings together expertise and resources encompassing three aspects critical to project success—TEs, nuclear science, and wireless sensors.

The project goal is to develop efficient and reliable TEGs based on high-efficiency nanostructured bulk materials that directly convert heat into electricity to power WSNs for nuclear applications. The benefit of self-powered WSNs goes beyond the cost savings of eliminating the need for cable installation and maintenance. Self-powered WSNs, as shown in Figure 1, will offer significant expansion in remote monitoring of nuclear facilities by providing important data on nuclear power plant equipment and component status during station blackouts or accident conditions; thus, WSNs will significantly improve reliability and safety in nuclear power plants and spent fuel storage facilities (Clayton et al. 2012).

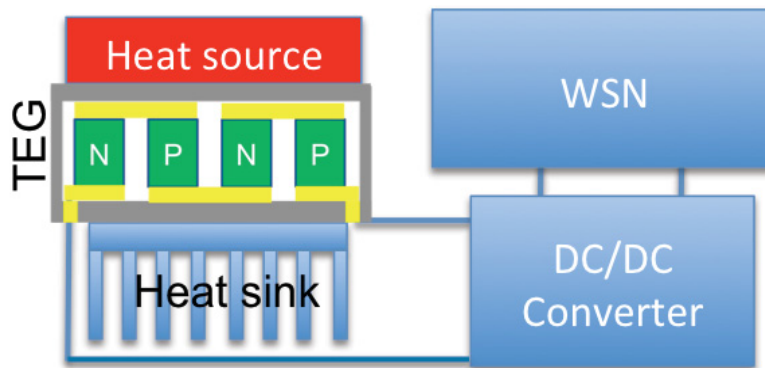


Figure 1. Schematic of self-powered WSN using TEG.

1.2 Problem Statement

The 2015 research activities of the project were focused on TEG material selection and development; study of radiation impact on structures and properties of TEG materials; TEG device simulation; and WSN power modeling and simulation based on the Institute of Electrical and Electronics Engineers

(IEEE) Communication Protocols 802.11 and 802.15.4. The 2016 INL research focus was on integrating TEG and WSN simulators with a direct-current-to-direct-current (DC-DC) converter as an interface. A DC-DC converter is essential to balance a wide range of analog, digital, and radio loads acting on the energy source. Also, the voltage level generated by TEGs under varying temperature conditions could be low, irregular, and insufficient to operate a WSN; therefore, DC-DC is required to boost the voltage to a desired level.

Most of the main problems of DC-DC converters used in a TEG system are related to impedance matching between the internal resistance of the TEG and the input resistance of the DC-DC converter. Figure 2 shows that the input power of a DC-DC converter has the largest value when impedance matching is achieved. This report addresses the issue associated with dynamic impedance matching under varying temperature conditions in the effort to integrate TEG and WSN.

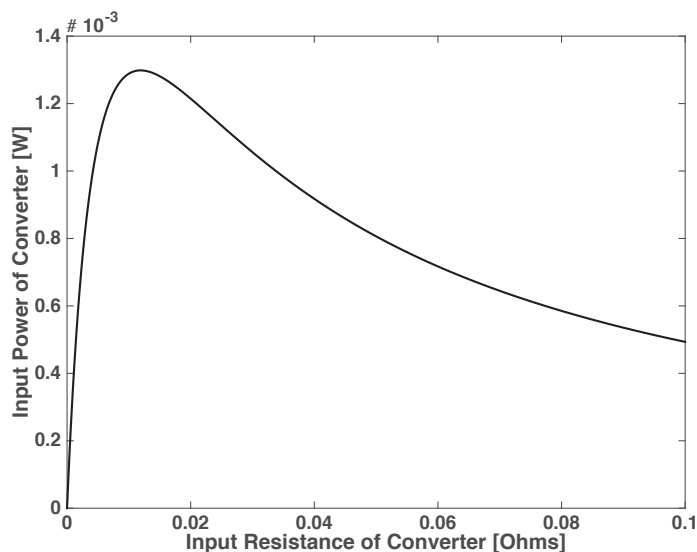


Figure 2. Input power of a DC-DC converter as a function of its input resistance.

1.3 Report Layout

This report focuses on integrating the TEG and WSN simulators developed at BSU and at INL, respectively. In this effort, dynamic impedance matching algorithms such as perturb and observe (P&O) and extremum-seeking control (ESC) algorithms will be implemented and compared to achieve maximum peak power tracking (MPPT). In addition, the report will summarize the study performed at BSU on profiling the behavior of a WSN prototype as it operates through different stages identified in Agarwal et al. (2015) and Agarwal (2011).

The report is laid out as follows:

Section 2 summarizes the TEG and WSN simulation effort.

Section 3 presents discussion on DC-DC converters, general principle of operation, and review of categories and topologies.

Section 4 describes the TEG and WSN integration effort with a DC-DC converter as the interface. The section presents information on MPPT and different approaches to achieve MPPT in a TEG-powered device under a varying temperature profile. The section also summarizes the results obtained from the two algorithms implemented to achieve MPPT.

Section 5 describes the experimental data collected on operation of a WSN prototype.

Section 6 summarizes the research effort on TEG-WSN integration and presents a path forward.

2. MODELING

In this section, the modeling effort associated with TEG and WSN is summarized.

2.1 Thermoelectric Modeling Overview

When a TEG is used in practical applications, it is used in combination with a heat exchanger or heat sink. Such a heat sink is required to effectively transfer heat from the hot source to the hot side of the TEG and to transfer heat from the cold side of the TEG to the cold sink, which is the ambient air in this situation. The modeling described here considers a TEG and a heat sink to transfer heat from the cold side of the TEG.

An analytical steady-state model was developed in a MATLAB[®] environment with the goal of maximizing the TE power produced by the TEG. The primary direction of heat transfer is from the pipe (heat source) to the ambient side; therefore, one-dimensional heat flow through the TEG and heat sink is considered as illustrated by Figure 3. The overall model consists of a TE model and a heat sink model.

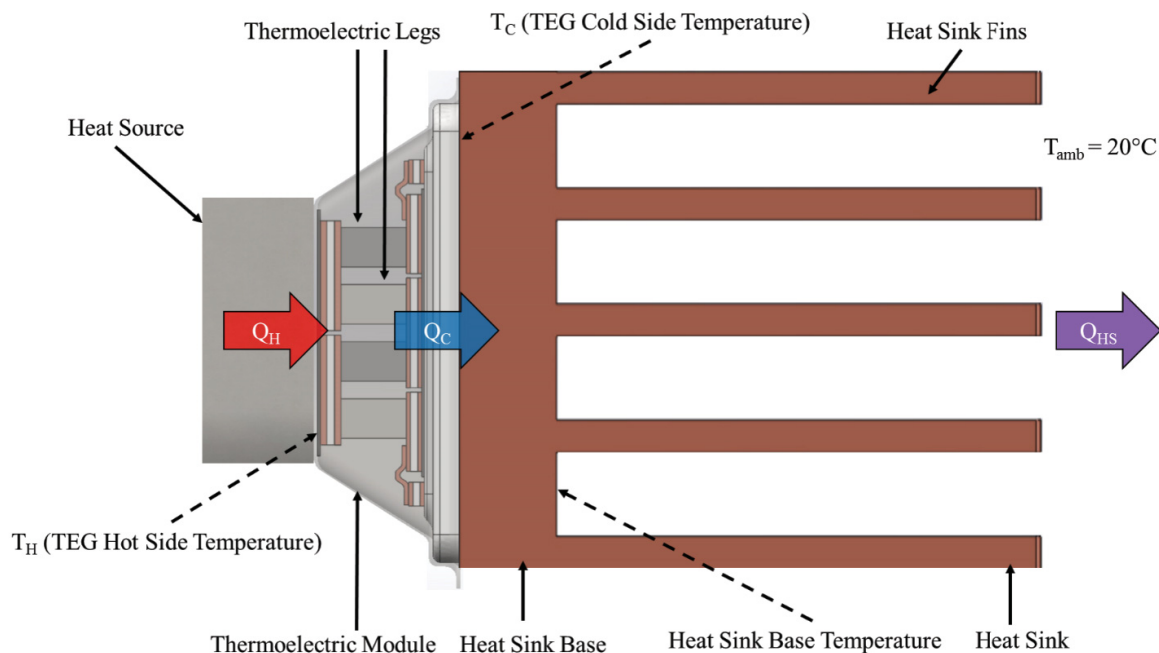


Figure 3. Heat transfer model accounting for the heat flow through the TEG and the heat sink, where Q_H is the heat flow into the hot side of the TEG, Q_C is the heat leaving the cold side of the TEG, and Q_{HS} is the heat flow from the heat sink to the ambient side. The heat sink plates are vertically oriented; the figure illustrates a top view.

2.1.1 Thermoelectric Model

A steady state 1-D TEG system model was developed to determine the heat flow through the TE module and power output from the TE device. The essential physical principle applied was the first law of thermodynamics as illustrated by Figure 3. A TEG consists of numerous TE couples; the model assumes that there are no temperature variations between the different TE unicouples. This assumption is made because the primary direction of heat flow is from the hot side of the uncouple to the cold side of the uncouple. In addition, any heat transfer from the exposed surfaces of the TE legs in the form of natural

convection or radiation was considered negligible because these surfaces can be insulated in practical applications.

The heat transferred into a TE leg was obtained by the following equation (Kumar et al. 2013):

$$Q_{h,p,n} = \text{abs}(\alpha_{p,n}) \cdot (T_{h,p,n}) \cdot I + K_{p,n}(T_{h,p,n} - T_{c,p,n}) - \frac{1}{2} I^2 \cdot R_{el,p,n} \quad (1)$$

The heat transferred from the cold side of the TE leg was obtained by the following equation:

$$Q_{c,p,n} = \text{abs}(\alpha_{p,n}) \cdot (T_{c,p,n}) \cdot I + K_{p,n}(T_{h,p,n} - T_{c,p,n}) + \frac{1}{2} I^2 \cdot R_{el,p,n} \quad (2)$$

where $Q_{h,p,n}$ is the heat transferred into the p-leg and n-leg, and $Q_{c,p,n}$ is the heat transferred from the cold side of the p-leg and n-leg.

The first terms on the right-hand side of *Equations (1) and (2)* account for the rate of Peltier heat generation at the boundaries of the legs, where $\alpha_{p,n}$ is the Seebeck coefficient of the two legs, $T_{h,p,n}$ is the hot-side temperature of the p-leg and the n-leg, and I is the current through the two legs, which are connected in series. The second term on the right side of *Equations (1) and (2)* accounts for the thermal conduction through the TE legs, where $T_{h,p,n}$ is defined as above, $T_{c,p,n}$ is the cold-side temperature of the two TE legs, and $K_{p,n}$ is the thermal conductance of the two separate legs obtained as follows:

$$K_{p,n} = \frac{\kappa_{p,n} \cdot A_{p,n}}{L_{p,n}} \quad (3)$$

where $\kappa_{p,n}$ is the thermal conductivity of the p- and n-legs, $A_{p,n}$ is the area of the two legs, and $L_{p,n}$ is the height of the TE legs. The third term on the right-hand side of *Equations (1) and (2)* accounts for any Joule heat produced in the TE legs. The model assumes that half the Joule heat is transferred to the hot side of the legs and the other half is transferred to the cold side, where I is defined as above and $R_{el,p,n}$ is the electrical resistance of each leg defined as follows:

$$R_{el,p,n} = \frac{\rho_{p,n} \cdot L_{p,n}}{A_{p,n}} \quad (4)$$

where $\rho_{p,n}$ is the electrical resistivity of the respective legs. The power output from each leg was found as follows:

$$P_{p,n} = Q_{h,p,n} - Q_{c,p,n} \quad (5)$$

The current I through the TE couple is obtained as follows:

$$I = \frac{\alpha_{TEC} \cdot (T_{h,p,n} - T_{c,p,n})}{R_{el,TEC} + R_{el,L}} \quad (6)$$

where α_{TEC} is the equivalent Seebeck coefficient of the uncouple given as follows:

$$\alpha_{TEC} = \alpha_p - \alpha_n \quad (7)$$

where α_p is the Seebeck coefficient of the p-leg and α_n is the Seebeck coefficient of the n-leg. $R_{el,TEC}$ is the total electrical resistance of the uncouple, and $R_{el,L}$ is the external electrical load resistance. To obtain maximum power, the external load resistance must be set equal to the total electrical resistance of the uncouple (Kim et al. 2015). It is important to note that each of the TE properties in the model accounts for any temperature variations. The TE properties of the Half-Heusler TE elements were obtained as a

function of temperature, as illustrated in Figure 4, by utilizing the temperature-dependent functions of an integral average using T_h and T_c as the limits of the integral to obtain the TE properties above.

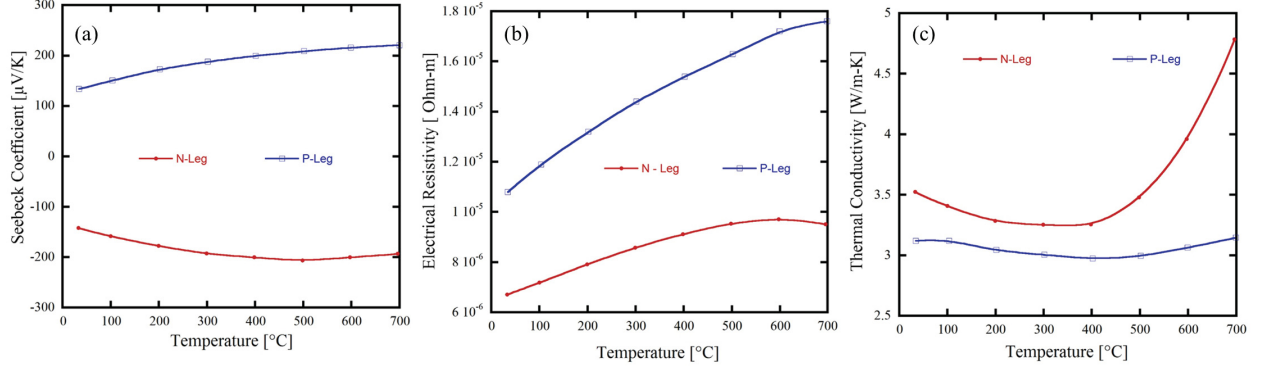


Figure 4. Temperature-dependent properties of the Half-Heusler p-leg and n-leg: (a) Seebeck coefficient, (b) electrical resistivity, and (c) thermal conductivity.

2.1.2 Heat Sink Model

A 1-D analytical steady state model is developed to predict the thermal performance of vertically oriented natural convection plate fin heat sinks. The primary direction of heat transfer is from the base of the heat sink to the ambient; consequently, the model assumes that there are no lateral variations in temperature along the heat sink base. The key parameter used to evaluate the performance of a heat sink is the thermal resistance of the heat sink defined as follows:

$$R_{th} = \frac{T_c - T_{amb}}{Q_{HS}} \quad (8)$$

where T_c is the cold-side temperature of the TEG, which is also the temperature of the heat sink surface attached to the cold side of the TEG. T_{amb} is the ambient temperature, and Q_{HS} is the heat flow through the heat sink.

The heat flow through the heat sink by heat convection was obtained as follows (Bar-Cohen et al. 2003):

$$Q_s = n_{fin} \cdot q_{fin} + h_{base} \cdot A_b \cdot (T_b - T_{amb}) \quad (9)$$

where n_{fin} is the number of fins, A_b is the unfinned base area, T_b is the heat sink base temperature, and h_{base} and q_{fin} are defined by *Equations (10) and (12)*.

The unfinned base area is treated as a vertical flat plate, and the convection heat transfer coefficient is obtained as follows:

$$H_{base} = 0.59 \cdot Ra_L^{1/4} \cdot k_a / L \quad (10)$$

where k_a is the thermal conductivity of air, L is the vertical length of the heat sink, and the Ra_L is obtained as follows:

$$Ra_L = g \cdot \beta \cdot \theta_b \cdot Pr \cdot L^3 / \nu^2 \quad (11)$$

where g is gravity, β is the coefficient of thermal expansion, θ_b is the temperature difference between the heat sink base and the ambient, Pr is the Prandtl number, and ν is the kinematic viscosity of the fluid.

The heat transfer from each of the individual plate fins, q_{fin} , is obtained as follows (Incropera and DeWitt 1981):

$$q_{fin} = M \cdot \tanh(m \cdot H) \quad (12)$$

where H is the height of the plate fins extruding in the horizontal direction and M and m are defined as follows:

$$M = \sqrt{h \cdot P \cdot k \cdot A_c} \cdot (T_b - T_{amb}) \quad (13)$$

$$m = \sqrt{(h \cdot P)/(k \cdot A_c)} \quad (14)$$

where k is the thermal conductivity of the fin material. P and A_c are defined below:

$$P = 2 \cdot L + 2 \cdot t \quad (15)$$

$$A_c = L \cdot t \quad (16)$$

where t is the fin thickness.

The convection heat transfer coefficient from non-isothermal plates (Bar-Cohen et al. 2003) is obtained as follows:

$$h_{fin} = \frac{k_a}{s} \cdot \left(\frac{576}{(\eta_{fin} \cdot El)^2} + \frac{2.873}{(\eta_{fin} \cdot El)^2} \right)^{1/2} \quad (17)$$

where s is the spacing between the plate fins, η_{fin} is the fin efficiency, and El , the Elenbaas number, is obtained as follows:

$$El = (g \cdot \beta \cdot \theta_b \cdot Pr \cdot s^4) / Lv^2 \quad (18)$$

Considering that the temperature difference between the heat sink and the ambient is of significant magnitude, radiation effects were considered in the heat-sink model. Radiation heat transferred from the outer surfaces of the heat sink was considered in the model, because these surfaces have a view factor of 1 with the ambient side temperature.

$$Q_r = A_r \cdot \sigma \cdot \varepsilon \cdot (T_{HS}^4 - T_{amb}^4) \quad (19)$$

where A_r is the heat sink area transferring heat by radiation to the ambient side, σ is the Boltzmann constant, ε is the emissivity of the heat sink material, and T_{HS} is the average heat sink temperature. It is important to note that the model uses absolute temperature values for the radiation analysis.

2.1.3 Combined Heat Transfer Model

The TE model was combined with the heat sink model to obtain a combined heat transfer model. The inputs into the heat transfer model are the TEG hot-side temperature (T_H) and the ambient temperature (T_{amb}). The combined model is solved by an iterative process, which requires that the heat leaving the cold side of the TEG (Q_c) match the heat flow through the heat sink (Q_{HS}). The convergence criterion was equal to 10^{-6} . When the convergence criterion is met, the model will solve for the cold-side temperature. Eventually, the model will output the heat flow through the TEG, while obtaining the cold-side temperature of the TEG and the power output of the TEG, as well as the operational current and voltage.

2.1.4 Heat Sink Optimization

The plate fin heat sink was optimized in order to obtain a minimal thermal resistance. The plate fin thickness, height, and packing fraction were optimized. The base area of the heat sink and TEG was chosen to be $4 \text{ cm} \times 4 \text{ cm}$, because this was a conventional base area of a TE module. The heat sink material was chosen to be copper, due to its high thermal conductivity and mechanical stability. It is interesting to note from *Equations (10) and (17)*, the heat convection coefficients are independent of the plate fin heights. The plate fin heights increase in the transverse direction to the primary direction of the buoyancy forces. However, the plate fin height will influence the fin efficiency. Because the fin material is copper, the fin height does not have a significant effect on the fin efficiency in the fin height optimization range considered. The thermal resistance is obtained for varied fin heights for different fin thicknesses. The thermal resistance approaches an asymptotic minimum as the fin height is increased as shown in Figure 5(a). A point of diminishing returns is selected as the height where the thermal resistance is $1.25 \times$ the value of the asymptotic minimum value. For the fin thicknesses 1 mm, 2 mm, 3 mm, and 4 mm, the point of diminishing returns was reached at fin heights of 0.13 m, 0.17 m, 0.19 m, and 0.2 m, respectively; therefore, 0.2 m was selected as the optimized plate height.

The fin thickness and fin packing fraction were optimized simultaneously using the plate height of 0.2 m. The plate thickness was varied from 1 mm to 4 mm, while the fin count was varied for each of the fin thicknesses in order to obtain the minimum thermal resistance. As illustrated by Figure 5(b), a fin thickness of 2 mm produces the least thermal resistance. Similarly, a fin packing fraction of 30% produced the least thermal resistance as demonstrated by Figure 5(c). The optimized heat sink dimensions are listed in Table 1.

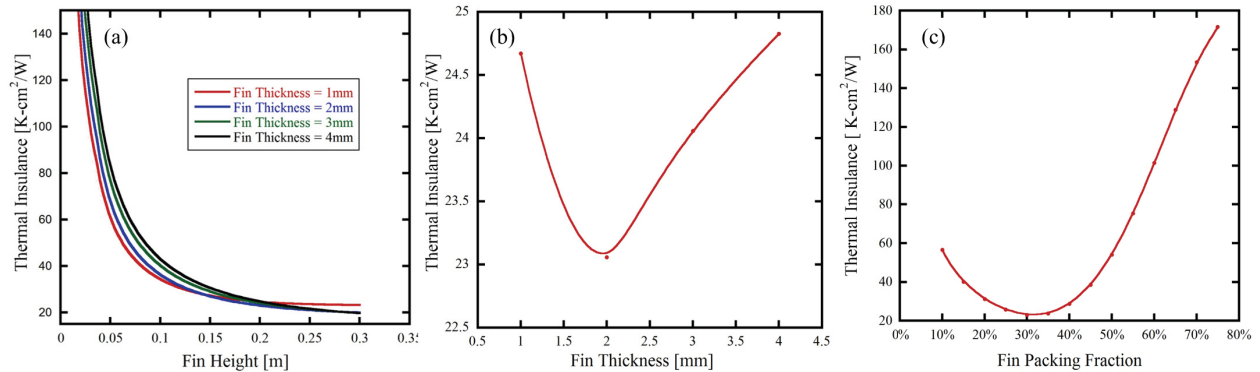


Figure 5.(a) Thermal Insulance for varied fin heights and fin thicknesses, (b) minimum thermal Insulance for varied fin thicknesses for a plate height of 20 cm, (c) thermal Insulance for varied packing fractions for a fin thickness of 2 mm and fin height of 20 cm.

Table 1. Optimized heat sink parameters.

Parameter	Value
Base Area	$4 \text{ cm} \times 4 \text{ cm}$
Base Thickness	1 cm
Fin Height (extruding from base)	20 cm
Fin Thickness	2mm
Fin Length (vertical)	4 cm
Fin Count	6

2.1.5 Thermoelectric Generator Optimization

The maximum TE power from a TEG is obtained when the thermal resistance of the TEG matches any external thermal resistance (Leonov and Fiorini 2007). Such a condition is required, based on obtaining the largest possible heat flow through the TEG, while having the largest possible temperature difference across the TEG. The thermal resistance of the TEG can be altered by changing the TE leg packing fraction or the TE leg height. The TEG was optimized by fixing the leg packing fraction at 15.75% and varying the n- and p-leg heights simultaneously. As illustrated by Figure 6, the TE power is maximized when the thermal resistance of the TEG matches that of the heat sink. The hot-side temperature was considered to be 200°C, because this was the temperature on the surface of a pipe where the device will be placed, and the ambient was equal to 20°C. The optimized TEG parameters are listed in Table 2.

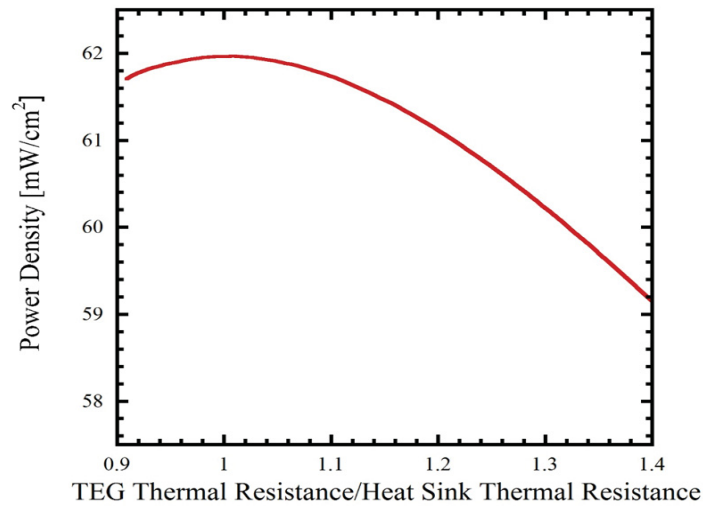


Figure 6. TE power density for varied TE leg heights from 1 mm to 1.8 mm for a leg packing fraction of 15.75%.

Table 2. Optimized TE module parameters.

Parameter	Value
Leg Area	1.5 mm × 1.5 mm
Leg Height	1.16 mm
Number of Couples	56
Leg Packing Fraction	15.75%

2.1.6 Thermoelectric Module Results

The optimized TEG heat sink design was used to obtain the power-current curves and the voltage-current curves for temperature differences of 400°C, 300°C, and 200°C between the hot side and the ambient side. For an optimized TEG heat sink design, the thermal impedance of the TEG matches that of the heat sink. When this condition is met, the temperature drop across the TEG will be half the temperature difference between the hot side and the ambient side. For an ambient temperature of 20°C

and hot-side temperatures of 420°C, 320°C, 220°C, the cold-side temperatures are 220°C, 170°C, and 120°C, respectively. TEG power results are obtained by varying the electrical load resistance $R_{el,L}$, which produces the TEG power-current curves illustrated in Figure 7(a). The TEG voltage results as a function of electrical current are shown in Figure 7(b).

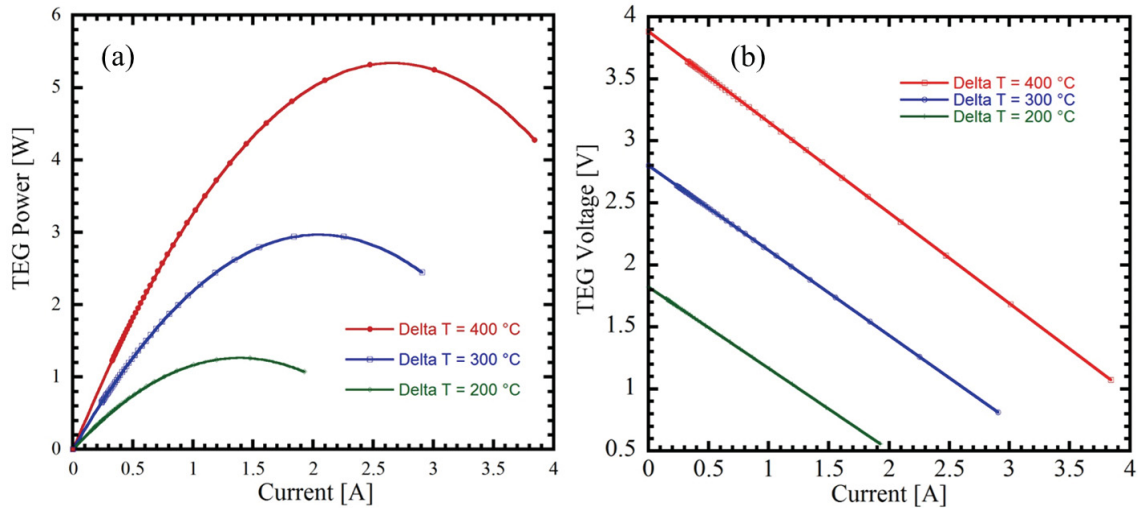


Figure 7. (a) TEG power output for varied load resistances that produce distinct currents at hot-side temperatures of 420°C, 320°C, and 220°C and an ambient temperature of 20°C. (b) TEG voltage as a function of current for varied load resistances at hot-side temperatures of 420°C, 320°C, and 220°C and an ambient temperature of 20°C.

A transient solution is obtained using the optimized TEG-heat sink device, by having a time-dependent hot-side temperature, while the cold-side temperature is held constant at 20°C. The hot-side temperature varies from 240 to 270°C over 30 minutes, and changes from 270 to 240°C over the next 30 minutes as shown by Figure 8(a). The TEG power results are illustrated in Figure 8(a) using the corresponding hot-side temperatures. The operational voltages and currents for maximum power are illustrated in Figure 8(b).

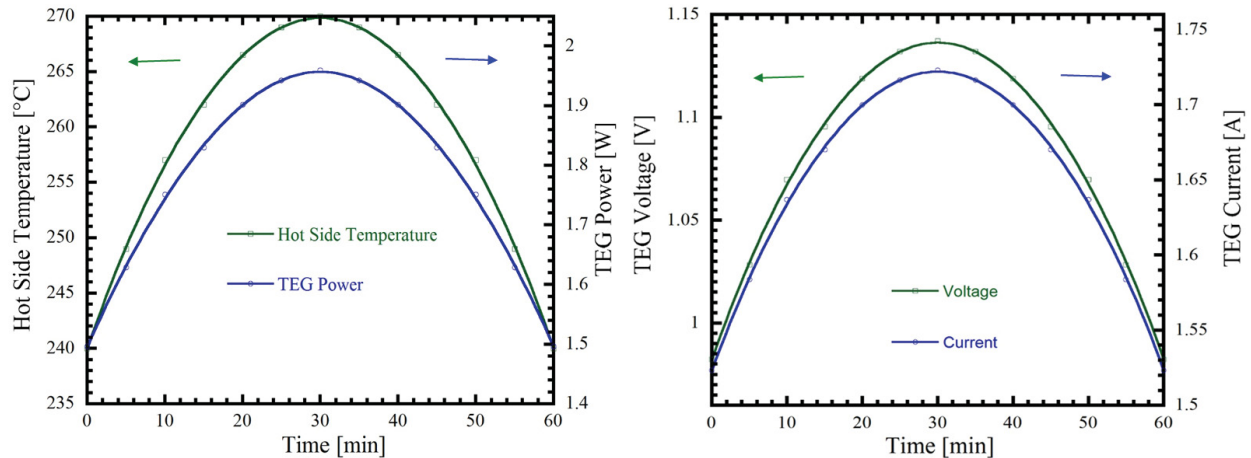


Figure 8. (a) Hot-side temperature variation with time and peak TEG power obtained when the respective hot-side temperature is used with an ambient temperature of 20°C. (b) Corresponding TEG voltage and current required for peak power in Figure (a).

2.2 Wireless Sensor Node Modeling

This subsection summarizes the WSN power modeling and simulation based on IEEE Communication Protocols 802.11 and 802.15.4 performed at INL. For details on rigorous stochastic modeling of a WSN, refer to Agarwal (2011) and Agarwal et al. (2015).

As part of the modeling effort, six different operational states of a WSN are identified (Agarwal 2011). Thus, the operational state space of a WSN is $\mathbf{S} = \{S_0, S_{1i}, S_{1e}, S_{1r}, S_2, S_3\}$ where

- (i) S_0 represents the SLEEP state during which the WSN is completely disconnected from the base station and from other WSNs
- (ii) S_{1i} represents the ACTIVE state when no event is detected
- (iii) S_{1e} represents the ACTIVE state when only a sensing-event occurs
- (iv) S_{1r} represents the ACTIVE state when only a receiving-event occurs, i.e., the WSN receives a packet of information from other WSNs and forwards or relays the information to the receiving WSN (or to the base station)
- (v) S_2 represents the ACTIVE state during which processing of event information is performed
- (vi) S_3 represents the ACTIVE state during which information is transmitted.

Each state in \mathbf{S} has a certain associated power consumption, which discharges the WSN battery. An additional energy cost is associated with transitions between states. Let $I_S = \{0, 1i, 1e, 1r, 2, 3\}$ denote the index for the possible states of the WSN. Based on modeling assumptions and the frequency of event occurrence, the WSN transitions to a particular state $S_k, k \in I_S$. The time duration a WSN spends in a particular state is not fixed, except for the sleep state, T_{S_0} , which is fixed (for the purpose of this research and can be easily converted to a random variable). Thus the time spent in each of the other states is considered to be random variables with mean value $\mu_k, k \in I_S$. After spending a random amount of time in a particular state, the WSN transitions to the next allowable state with transition probability $P_{ij}, \neq j$. Thus, to describe the transition of the WSN from one state to another state, the following information is required: (i) the present state of the WSN and (ii) the random amount of time it spends in the present state. Fundamentally, the operational behavior of a WSN shown in Figure 9 can be captured using the following probability transition matrix \mathbf{P} .

$$\mathbf{P}: \begin{array}{c} S_0 \\ S_{1i} \\ S_{1e} \\ S_{1r} \\ S_2 \\ S_3 \end{array} \begin{array}{cccccc} S_0 & S_{1i} & S_{1e} & S_{1r} & S_2 & S_3 \\ \left[\begin{array}{cccccc} 0 & 1 - \alpha - \beta + \alpha\beta & \alpha & (1 - \alpha)\beta & 0 & 0 \\ 1 & 0 & 0 & 0 & 0 & 0 \\ 0 & 0 & 0 & 0 & 1 & 0 \\ 0 & 0 & 0 & 0 & 0 & 1 \\ 0 & 0 & 0 & 0 & 0 & 1 \\ 1 & 0 & 0 & 0 & 0 & 0 \end{array} \right] \end{array} \quad (20)$$

The entries of the matrix \mathbf{P} must satisfy the following constraints:

$$0 \leq p_{ij} \leq 1, \quad i, j \in \mathbf{S} \quad (21)$$

$$\sum_{j \in \mathbf{S}} p_{ij} = 1, \quad i \in \mathbf{S} \quad (22)$$

In Equation (20) α is the probability of a sensing event occurring, and β is the probability of a relay event occurring.

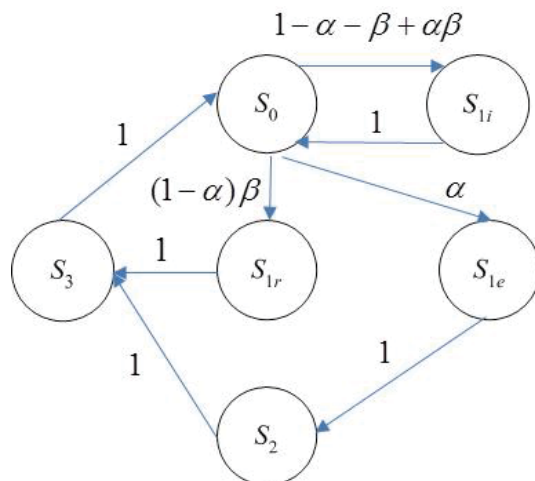


Figure 9. State transition diagram (Agarwal 2011).

This transition of a WSN from its present state to the next allowable state acts as a variable load across the DC-DC converter (discussed in Section 3) to which the TEG is connected. This enables computation of load information across the TEG power device.

3. DC-DC CONVERTERS

A DC-DC converter is an electronic circuit or electromechanical device that converts a source of direct current (DC) from one voltage level to another. One of the most popular classification methods groups converters by the existence of transformers, which are sometimes incorporated into the DC-DC converter, so as to achieve DC isolation between the input and output of the converter. Converters with transformers are referred to as isolating converters; ones without transformers are labeled as non-isolating converters (Li 2011).

Non-isolated converters: There are three basic types of non-isolated converters, namely, buck, boost, and buck-boost. For a converter, the switching transistors (T_r) and diodes (D) are designed to open and close such that the inductor (L) and capacitor (C) either store extra power or release power to maintain the output voltage within a desired range. The buck converter reduces the output voltage relative to the input voltage of the power generator (i.e., photovoltaic module), and the output current increases accordingly. In contrast, the buck converter increases the output voltage relative to the input voltage of the power module. Finally, the buck-boost converter is a combination of the buck converter and the boost converter, which can both reduce and increase the voltage as needed. The circuit diagrams of these converters are presented in Figure 10 (Jahanbakhsh 2012, Kotak and Tyagi 2013). Furthermore, by manipulating these basic converters (for instance, a cascade connection of converters), various converter circuits can be built to meet specific requirements (Li 2011). The transfer function controlling the input-output voltage/current relationship for buck, boost, and buck-boost converters in terms of duty-cycle is summarized in Table 3.

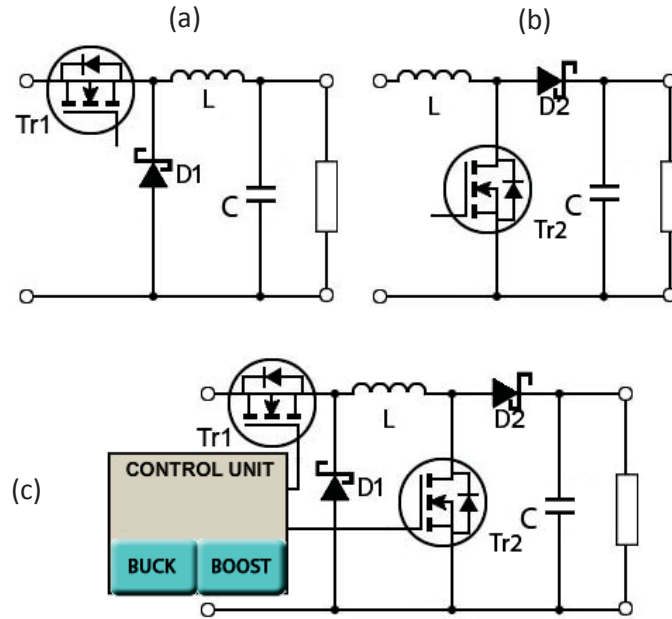


Figure 10. Circuit diagrams for the buck (a), boost (b), and buck-boost (c) converters (Jahanbakhsh 2012, Kotak and Tyagi 2013).

Table 3. Transfer function of different converter topology.

Converter Topology	Transfer Function
Buck	D
Boost	$\frac{1}{1 - D}$
Buck-Boost	$-\frac{D}{1 - D}$

Isolated converters: When a large step-up or step-down conversion ratio in voltage is required, the transformer is included to allow better converter optimization. Figure 11 shows the isolating DC-DC buck converter, which is well suited for applications that require high output current.

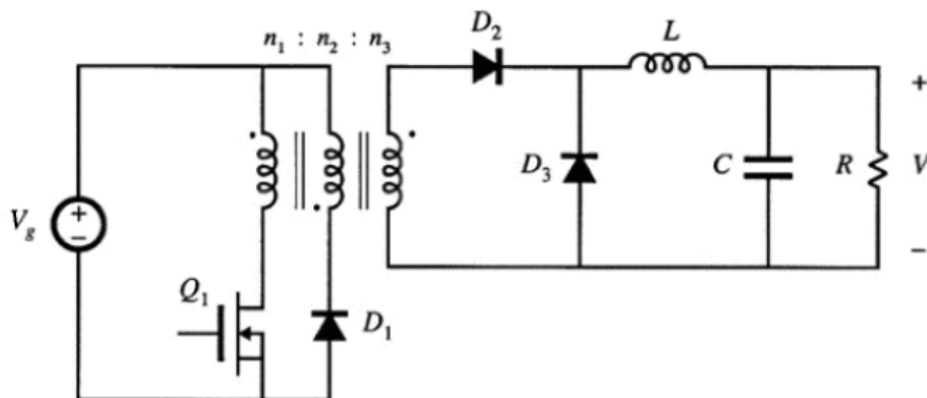


Figure 11. Simplified circuit diagram of an isolating DC-DC buck converter (Li 2011).

Switching frequency: A DC-DC converter's switching frequency should be designed taking into account the power level, cooling method, and application requirements. An increase in switching frequency leads to faster response of the system but will also increase the switch loss and magnetic core loss. Almost all modern DC-DC converters utilize a pulse-width-modulation signal as the switching control signal because of its advantage of linear control over the load power.

Conduction modes of converter: The conduction modes of a converter are (1) continuous conduction mode wherein the current fluctuates but never goes down to zero, which is preferable for high power application and (2) discontinuous conduction mode wherein the current fluctuates during the cycle, going down to zero each cycle, which is better for a low-power application where efficiency is necessary. The continuous conduction mode can be achieved by picking a large inductor to increase its discharging time to avoid dropping the current to zero.

4. THERMOELECTRIC GENERATION AND WIRELESS SENSOR NODE INTEGRATOR

4.1 Maximum Peak Power Tracking

The TEG simulation/modeling generates a P-V characteristic curve. The necessary condition that must be satisfied to achieve maximum power generated by a TEG is:

$$\frac{dP_{TEG}}{dV_{TEG}} = 0 \quad (23)$$

where P_{TEG} in watts (W) and V_{TEG} in volts (V) are the TEG output power and voltage, respectively. As observed in Figure 12, the peak value of the TEG changes as the temperature gradient between the hot side and the cold side changes over time. To operate around peak power generated by the TEG, the operating duty cycle (D) of a DC-DC booster circuit is adjusted by MPPT algorithms. The output of an MPPT algorithm changes the D by using a pulse width modulation controller. There are many MPPT algorithms published in the literature (Bendib et al. 2015). In this report, only two MPPT algorithms are discussed and implemented. They are (1) a P&O algorithm and (2) an ESC algorithm.

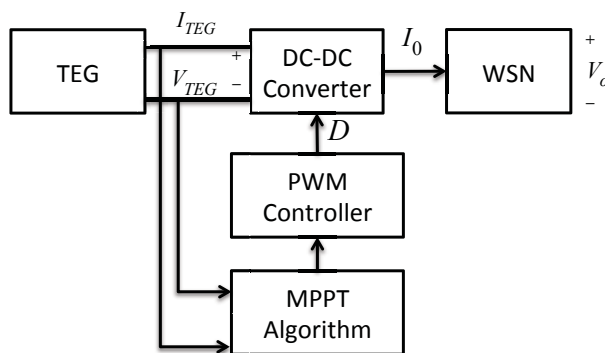


Figure 12. Schematic illustration of MPPT in a TEG-powered WSN.

4.2 Perturb and Observe Algorithm

The P&O algorithm (Piegari and Rizzo 2010, Algendy et al. 2012, Jiang et al. 2013, Lian et al. 2014) is widely used in commercial products and is the basis of the largest part of the most sophisticated algorithms presented in the literature (Bendib et al. 2015).

The P&O algorithm operates periodically by perturbing the operating voltage point (V_{TEG}) of the TEG and observing the power variation in the TEG to determine the change in direction of the reference voltage. For instance, if the operating voltage of the TEG V_{TEG} is perturbed in a given direction and if the

power drawn from the TEG increases, this means that the operating point has moved toward the maximum peak power (MPP), and therefore, the operating voltage must be further perturbed in the same direction. Alternatively, if the power drawn from the TEG decreases, the operating point has moved away from the MPP, and therefore, the direction of the operating voltage perturbation must be reversed. Figure 13 is a flow chart of the P&O algorithm. With this algorithm, the operating voltage V_{TEG} is perturbed at every MPPT cycle. As soon as the MPP is reached, V_{TEG} will oscillate around the ideal operating voltage, defined as V_{MPP} . This causes a power loss as it on the step width of the perturbation.

The performance of the P&O algorithm is limited by two main drawbacks. First, when the operating voltage V_{TEG} reaches the vicinity of V_{MPP} , the operating point oscillates around V_{MPP} , resulting in unending oscillation in the output power. This can be explained using Figure 14. Under steady state operation, assume that the operating voltage has moved from Point 1 to Point 2 in Figure 14 and the decision has to be made at Point 3 of the MPPT cycle. The values of dP and dV are computed. As $dP = (P_2 - P_1) > 0$ and $dV = (V_2 - V_1) > 0$, the algorithm decreases the duty cycle (D); hence the operating voltage moves to Point 3. At Point 3, as $dP = (P_3 - P_2) < 0$ and $dV = (V_3 - V_2) > 0$, the algorithm increases the value of D ; thereby the operating voltage moves back to Point 2. At Point 2, as $dP = (P_2 - P_3) > 0$ and $dV = (V_2 - V_3) < 0$, the algorithm decreases the value of D , and thereby the operating point moves to Point 1. At Point 1, as $dP = (P_1 - P_2) < 0$ and $dV = (V_1 - V_2) < 0$, the algorithm decreases the D , and thereby, the operating point moves back to Point 2. In this pattern, the algorithm makes the operating point oscillate between the three points surrounding V_{MPP} .

As a result, the energy yield is reduced, and hence there is a drop in the efficiency. Secondly, P&O is prone to losing its operating direction, i.e., it cannot cope with the change in the temperature conditions and causes the operating voltage V_{TEG} to diverge from the V_{MPP} locus. This divergence also results in energy loss. Several improvements to the P&O algorithms have been proposed in order to reduce the number of oscillations around the V_{MPP} (Bendib et al. 2015).

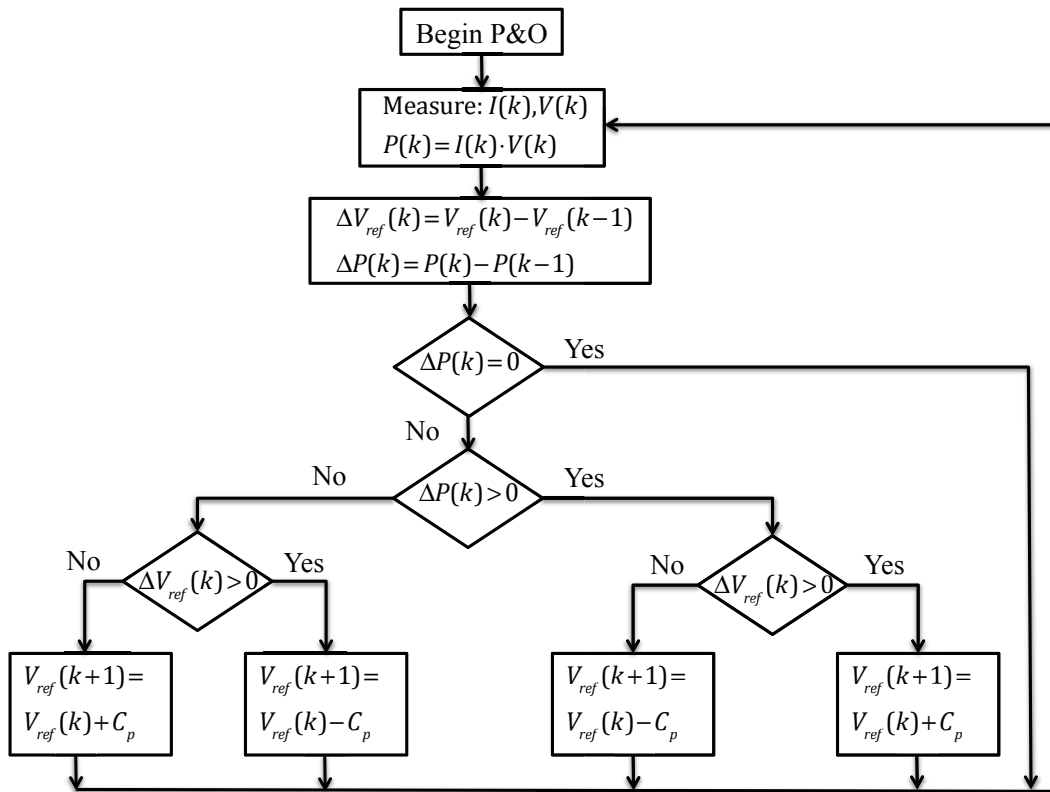


Figure 13. Flow chart of the P&O MPPT algorithm.

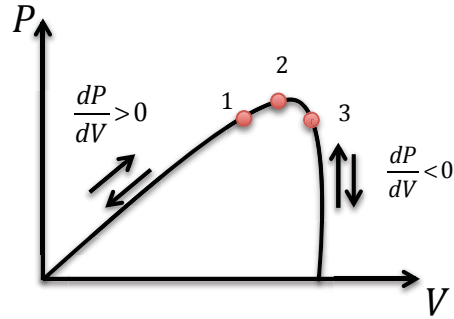


Figure 14. Illustration of oscillation in the P&O algorithm.

4.3 Extremum Seeking Control Algorithm

The ESC algorithm is a well-established adaptive control approach that reaches the control target via a filtered and a driving signal. Some of the applications of ESC are in nonlinear controls and nonlinear minimum and maximum localization.

The basic operating principle of the ESC algorithm is shown in Figure 15, which comprises an integrator, a differentiator, a logic circuit, and an amplifier (Yau and Wu 2011; Leyva et al. 2006). The ESC algorithm is then applied to track the MPP, i.e., to locate the maximum power point. The equation describing the system behavior is governed by an integrator,

$$\frac{dx}{dt} = K\varepsilon \quad (24)$$

where $\varepsilon = \pm 1$ and K is a constant; a differentiator,

$$g = \frac{dy}{dt} \quad (25)$$

and a logic circuit subsystem that implements the following function

$$\begin{aligned} &\text{change the sign of } \varepsilon && \text{if } g < 0 \\ &\text{keep the sign of } \varepsilon && \text{if } g > 0 \end{aligned} \quad (26)$$

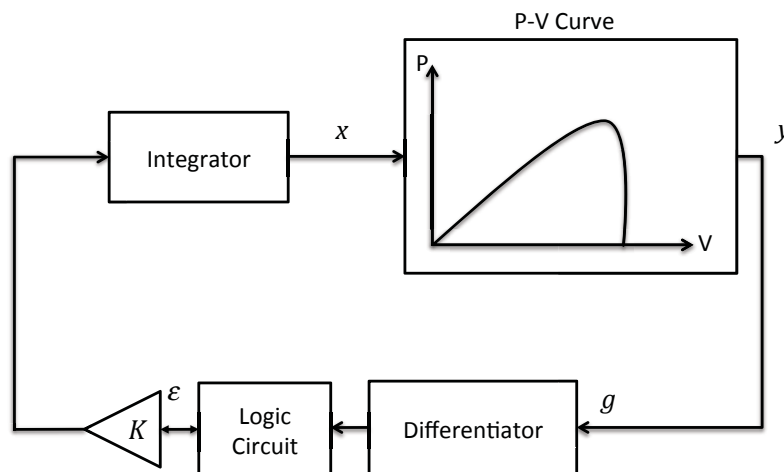


Figure 15. A block diagram of an ESC control system.

Case 1: Vector a in **Error! Reference source not found.** describes a movement where both horizontal and vertical components are increasing, i.e., $(dx/dt)|_{t^-} > 0$ and $(dy/dt)|_{t^-} > 0$, which results in a trajectory directed toward the optimal point from its left side. Therefore, the controller must keep the sign of the horizontal variation, i.e., $(dx/dt)|_{t^+} = K$.

Case 2: Vector c describes a movement where both horizontal and vertical components are decreasing, i.e., $(dx/dt)|_{t^-} < 0$ and $(dy/dt)|_{t^-} < 0$, which results in a trajectory directed away from the optimal point from its left side. Therefore, the controller must keep the sign of the horizontal variation, i.e., $(dx/dt)|_{t^+} = K$.

Case 3: Vector d illustrates a movement where the horizontal component is increasing while the vertical component is decreasing, i.e., $(dx/dt)|_{t^-} > 0$ and $(dy/dt)|_{t^-} < 0$, which represents a movement going away from the maximum point toward the right. In this case, the control action will change the sign of the horizontal variation. Therefore, $(dx/dt)|_{t^+} = -K$.

Case 4: Vector b corresponds to a movement where the horizontal component is decreasing while the vertical component is increasing, i.e., $(dx/dt)|_{t^-} < 0$ and $(dy/dt)|_{t^-} > 0$, which represents a movement going away from the maximum point toward the right. Therefore, control action in this case will change the sign of the horizontal variation. Therefore, $(dx/dt)|_{t^+} = -K$.

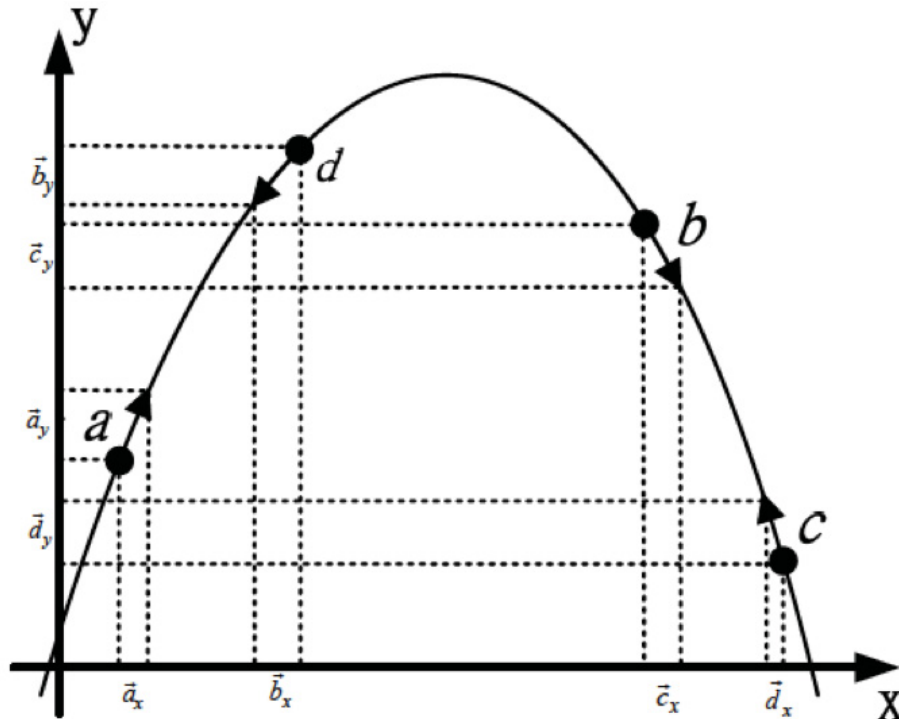


Figure 16. Illustrative cases of an ESC mechanism (Leyva et al. 2006).

Since $dy/dx = (dy/dt)/(dx/dt)$, Cases 1–4 can be expressed in compact form as follows:

$$\left. \frac{dx}{dt} \right|_t = K \quad \text{if } \left. \frac{dy}{dx} \right|_t > 0 \quad (27)$$

$$\left. \frac{dx}{dt} \right|_t = -K \quad \text{if } \left. \frac{dy}{dx} \right|_t < 0 \quad (28)$$

Equations (27) and (28) can also be reduced to only one expression:

$$\frac{dx}{dt} = K \text{sign} \left(\frac{dy}{dx} \right) \quad (29)$$

Note that the algorithm measures the sign of dy/dt , whereas the resulting dynamics are governed by dy/dx . Also, it can be observed in Equation (29) that the equilibrium point $dx/dt = 0$ will correspond to an extremum of the $x - y$ curve in **Error! Reference source not found.**, where $dy/dx = 0$. Note also in Equation (29) that the system dynamics change with the constant slope, which can be either positive or negative, depending on the sign of the slope of the $x - y$ curve.

4.4 Implementation of Maximum Peak Power Tracking Algorithms and Results

The two MPPT algorithms discussed above are implemented in a MATLAB® environment. Data from the TEG modeling effort at BSU were used as input to the MATLAB® DC-DC controller model with embedded MPPT models. For the P&O MPPT algorithm a MATLAB® built-in model was utilized, and for the ESC MPPT algorithm the approach presented in Philip et al. (2013) was implemented.

The experimental output data on P-I curves were obtained from BSU. The experimental data were in agreement with the TEG simulation model also developed at BSU. The MPP experimental data at hot-side temperatures of 350°C, 400°C, and 450°C were recorded and are shown as black circles in Figure 17. Using the MATLAB® P&O implementation, the MPP was estimated for each temperature profile. The estimated MPP using the P&O algorithm is shown as red circles in Figure 17. As depicted in Figure 17, accuracy of the MPP estimation using the P&O algorithm decreases as the temperature of the hot side increases. Stabilizing (i.e., reducing oscillation around MPP) the P&O algorithm as the hot-side temperature increases is cumbersome and results in underperformance of the algorithm.

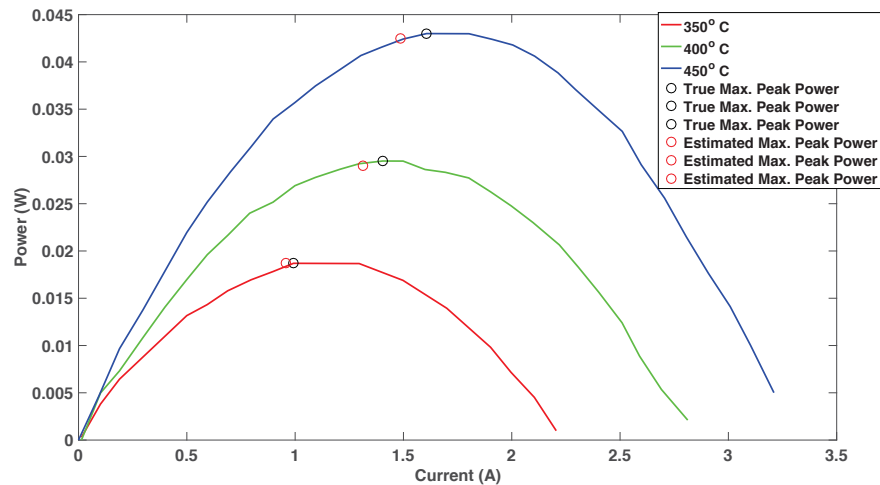


Figure 17. MPP estimated using P&O algorithms at different hot-side temperatures.

As described in Section 4.2, the performance of the P&O algorithm is limited due to oscillation of the estimated peak power around the MPP, which leads to a less accurate estimation of the MPP. To address this limitation of the P&O algorithm, another MPPT algorithm, the ESC algorithm shown in **Error! Reference source not found.**, was implemented on the same data set. Based on averaging analysis, the frequency of the perturbation signal, denoted ω , is set to be large with respect to the perturbation gain, denoted by k . The value of ω is selected to be higher than the high-pass filter frequency, denoted as ω_h , to eliminate unexpected oscillation. The details can be interpreted from the numerical analysis of the MPP with the ESC algorithm summarized in Appendix A. The parameters used for the ESC implementation with sine wave dither signal are summarized in

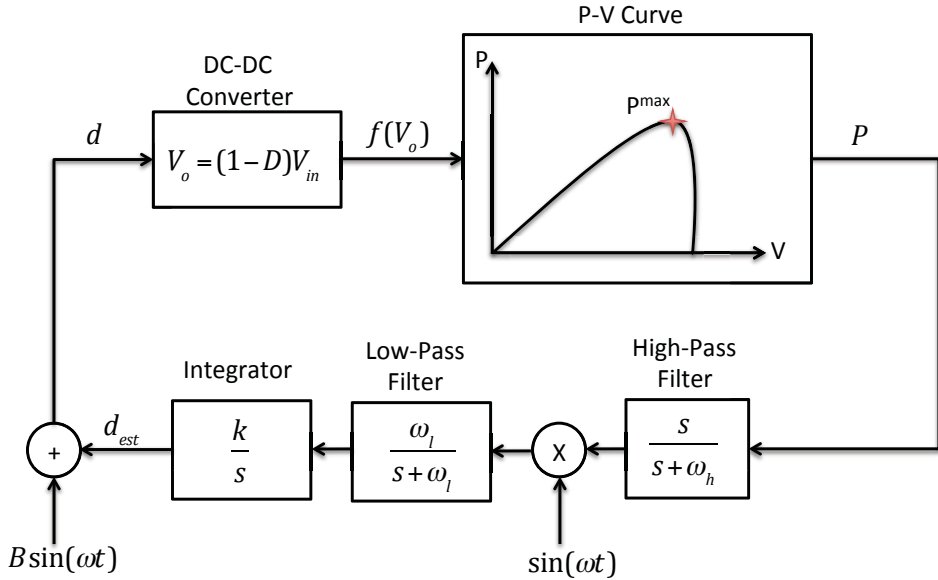


Figure 18. Block diagram of a sine wave dithered ESC algorithm.

Table 4. The results obtained using the ESC and P&O algorithms on the same data set are summarized in Table 5.

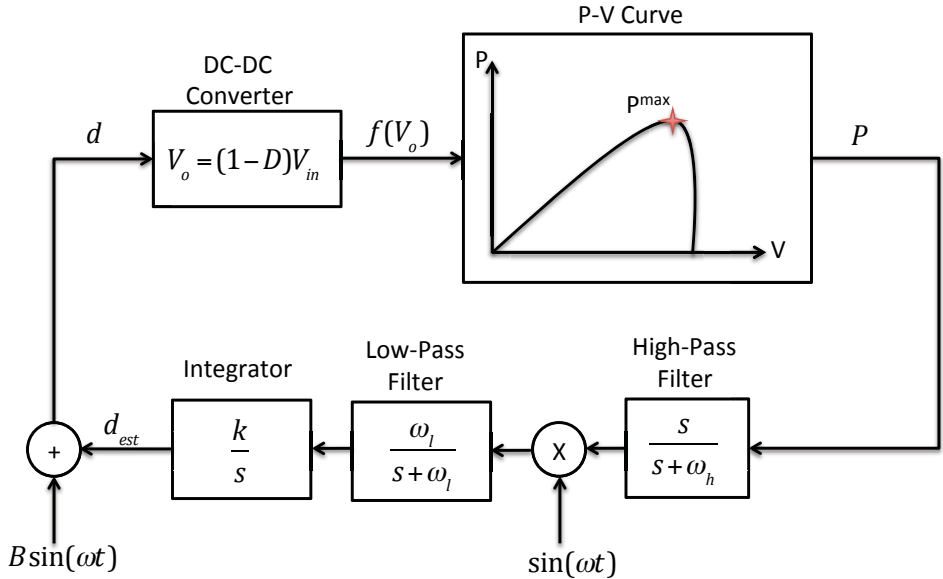


Figure 18. Block diagram of a sine wave dithered ESC algorithm.

Table 4. ESC parameter values.

High-pass frequency $\omega_h(\text{Hz})$	Perturbation frequency $f(\text{Hz})$	Integration gain k	Perturbation amplitude B
1.5	25	-100	50

Table 5. Comparison of estimated MPP using P&O and ESC algorithms.

Temperature (C)	Theoretical P(W)	P&O P(W)	ESC P(W)	Fixed duty cycle P(W)
450	0.04299	0.04221	0.04280	0.03680
400	0.02952	0.02876	0.02906	0.02704
350	0.01869	0.01814	0.01834	0.01576

Table 5 highlights improved performance of the ESC algorithm over the classical P&O algorithm in terms of accuracy as a function of time. In our research experience, stabilizing the performance of the ESC algorithm was simple compared to the P&O algorithm. Therefore, this MPPT algorithm would be implemented during the integration effort of the TEG and WSN hardware.

5. EXPERIMENTAL DATA ON WIRELESS SENSOR NODE

BSU is working on a TEG-powered WSN design and development. Different WSN elements such as a microprocessor, a micro SD storage device, and a transceiver were procured and assembled on a breadboard. Powering them via a battery source and measuring their response time and voltage allowed evaluation of the performance of the WSN elements. Figures 19–21 show the response time and voltage performance of each element.

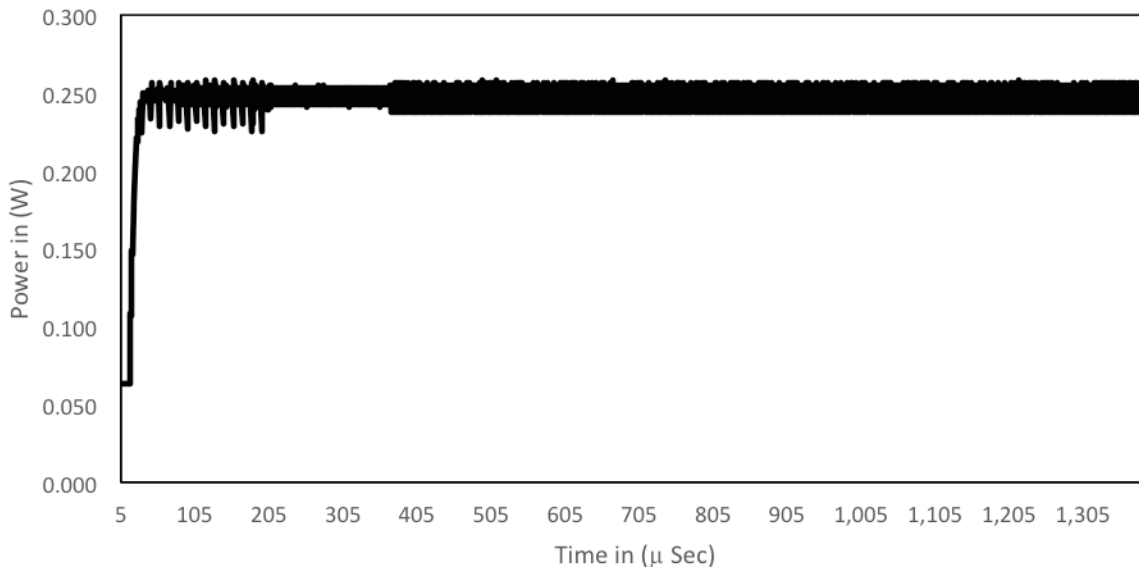


Figure 19. Response time and voltage measured across a micro-controller.

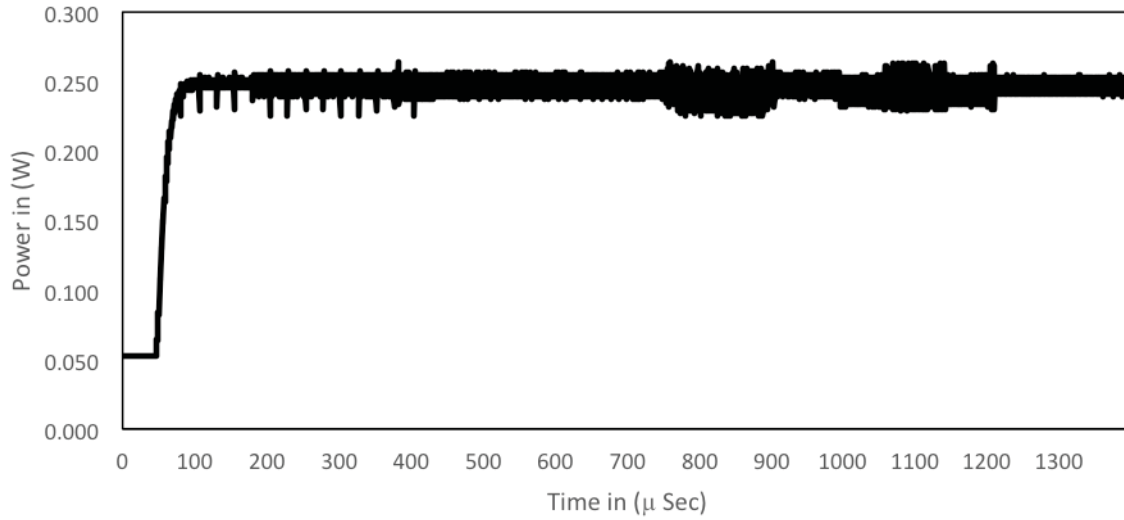


Figure 20. Response time and voltage measured across a microSD storage device.

Figure 21 shows the response time and voltage performance of a transceiver. As can be seen in Figure 21, significant oscillation is observed in the beginning as the transceiver attempts to settle down. This observation is important while evaluating transceiver performance when integrated with other WSN elements. Figure 22 shows the response time and voltage performance of a fully assembled WSN.

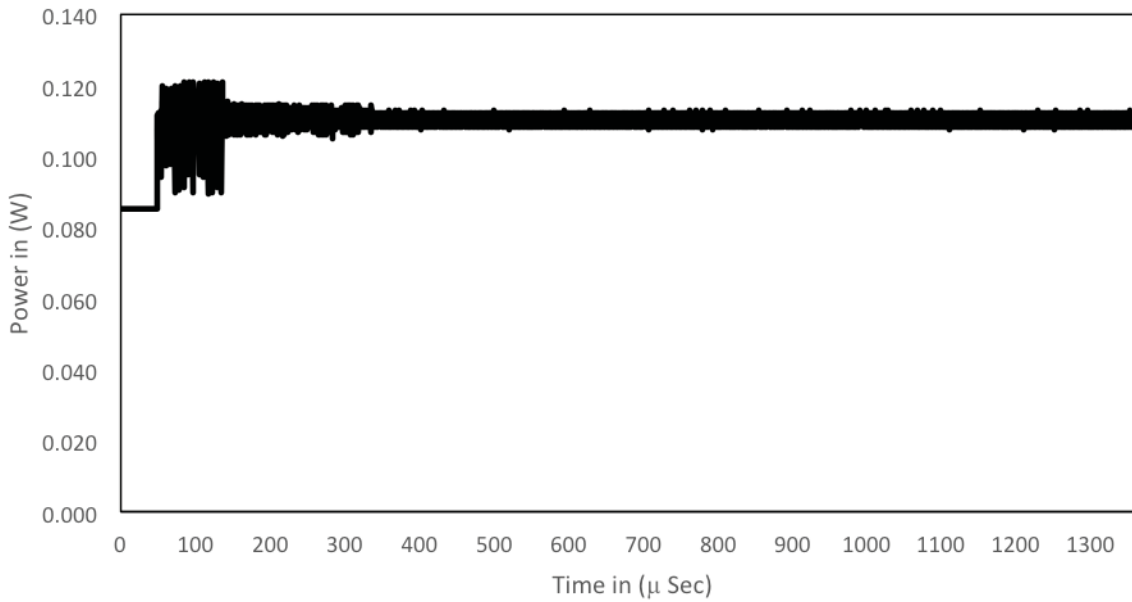


Figure 21. Response time and voltage measured across a transceiver based on IEEE 802.15.4 communication protocol.

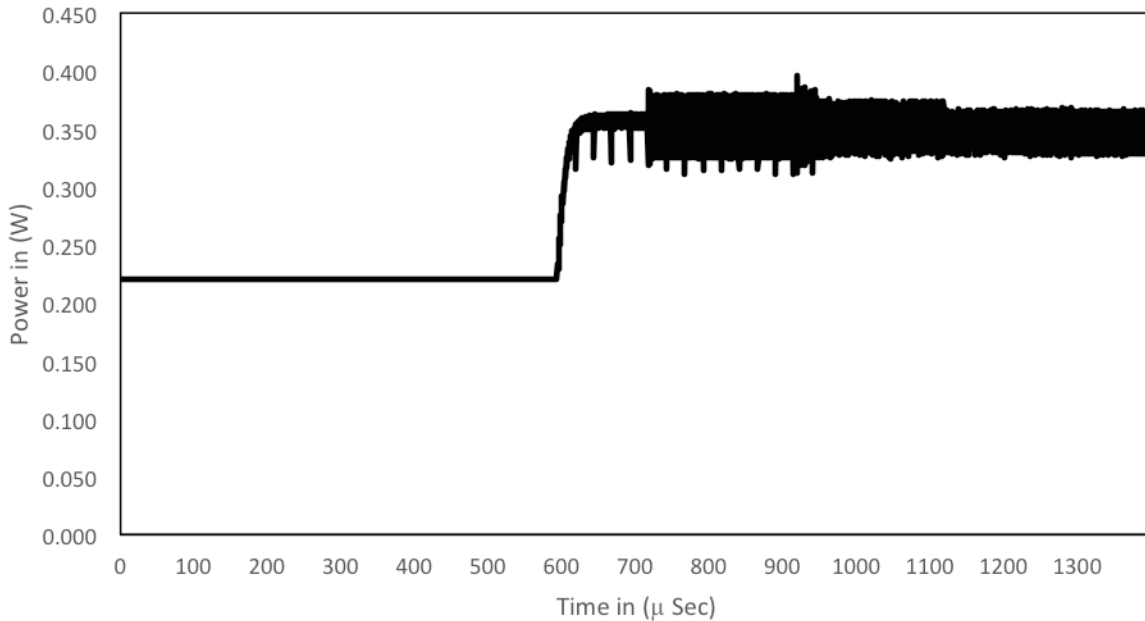


Figure 22. Response time and voltage measured across an assembled WSN.

To measure an accurate response of a WSN transitioning through different operational states, a 1-Ohm resistor is connected across the node and voltage is measured across the resistor to obtain the exact current value. Figure 23 shows the current profiling of a WSN across 1-Ohm resistor. Observing the rise and fall in the current value identifies different states of a WSN, and they map exactly with the time instant when the WSN transitions through the states.

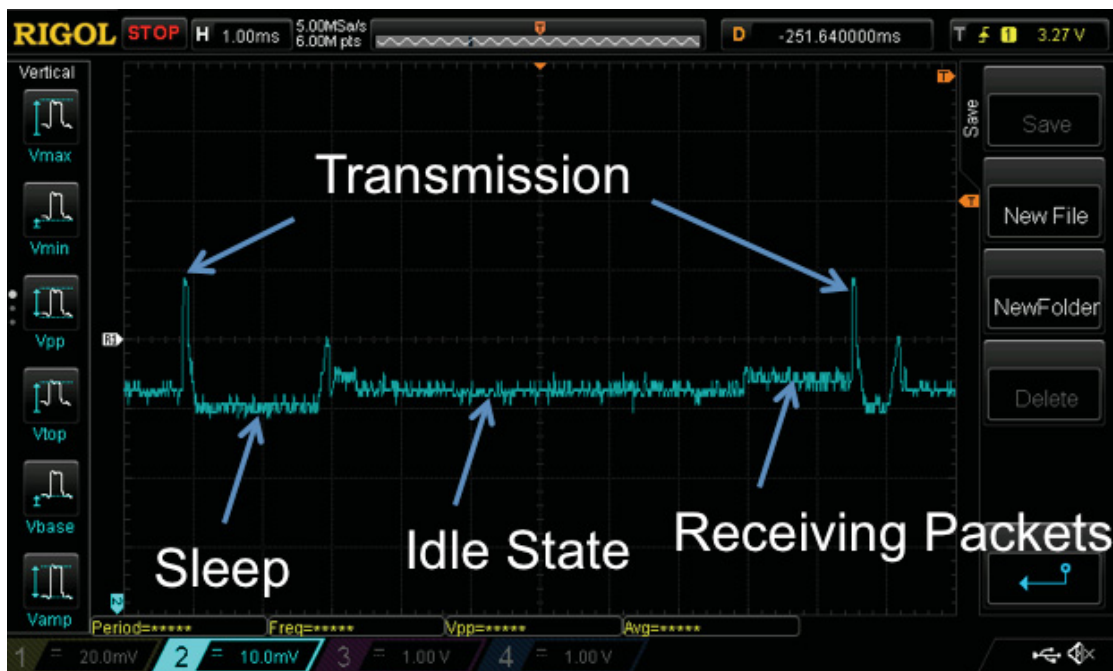


Figure 23. Response of a WSN recorded as it transitions through different operational states defined in the state space S .

6. CONCLUSIONS AND FUTURE WORK

This report describes the integration of TEG and WSN simulators developed independently at BSU and at INL, respectively. A DC-DC converter was used as an interface to integrate a TEG and a WSN. The purpose of the DC-DC converter was to regulate the output voltage of the TEG as per the demand of different elements of a WSN.

One important challenge that was addressed in this integration effort was MPPT. Under varying temperature conditions, the output of the TEG varies and so does its peak power output. It is essential to operate a TEG-powered WSN around its MPP to achieve optimal performance of a self-powered WSN. To achieve MPPT, two algorithms, P&O and ESC, were implemented in a MATLAB® environment. P&O is a widely used MPPT algorithm. Due to its limitation of inefficiency and stabilization around MPP, the ESC algorithm was implemented. In this research, a sine wave dithered ESC algorithm was implemented. It was found that the sine wave dithered ESC algorithm was stable around MPP and performed better than the P&O algorithm. In addition, the stability of the ESC algorithm was demonstrated via numerical analysis.

In a parallel effort, BSU was working on a TEG-powered WSN design and development. As a first step in this effort, a WSN was developed on a breadboard by assembling different elements of the WSN, such as a microprocessor, storage, and a transceiver. The performance of each element and integrated WSN was tested in a laboratory. The prototype provided an advantage to configure as per the requirements.

As part of future research, the focus is to enhance the design and development of TEG-powered WSNs. Based on integrator effort, the ESC MPPT algorithm will be implemented in TEG-powered WSNs for MPPT and to achieve optimal performance.

7. REFERENCES

- Agarwal, V., 2011, *Foundation for Power Management in Battery Powered Interconnected Wireless Sensor Networks*, Ph.D. Thesis: Purdue University, West Lafayette.
- Agarwal, V., J. Richardson, and Y. Zhang, 2015, *Wireless Sensor Network Power Profiling Based on IEEE 802.11 and IEEE 802.15.4 Communication Protocols: Modeling and Simulation*, INL/EXT-15-37005, Idaho National Laboratory, October 2015.
- Algendy, M. A., B. Zahawi, and D. J. Atkinson, 2012, "Assessment of perturb and observe MPPT algorithm implementation techniques for PV pumping applications," *IEEE Transactions on Sustainable Energy*, Vol. 3, No. 1, pp. 21–33.
- Bar-Cohen A, M. Iyengar, and A. D. Kraus, 2003, "Design of Optimum Plate-Fin Natural Convective Heat Sinks," *Journal of Electronic Packaging*, Vol. 125, No. 2, pp. 208–216.
- Bendib, B., H. Belmili, and F. Krim, 2015, "A survey of the most used MPPT methods: Conventional and advanced algorithms applied for photovoltaic system," *Renewable and Sustainable Energy Reviews*, Vol. 45, pp. 637–648.
- Clayton, D.A., W.H.J Andrews and R. Lenarduzzi, 2012, *Power Harvesting Practices and Technology Gaps for Sensor Networks*, ORNL/TM-2012/442, Oak Ridge National Laboratory, September 2012.
- Incropera, F. and D. DeWitt, 1981, *Fundamentals of Heat Transfer*, Wiley, New York.
- IEEE Std 802.15.4-2006, "Wireless Medium Access Control (MAC) and Physical Layer (PHY) Specifications for Low-Rate Wireless Personal Area Networks (WPANs)," Institute of Electrical and Electronics Engineers, 2006, September 8, 2006.
- IEEE Std 802.11-2007, "Wireless LAN Medium Access Control (MAC) and Physical Layer (PHY) Specifications," Institute of Electrical and Electronics Engineers, June 12, 2007.
- Jahanbakhsh, D., 2012, *Implementation of DC-DC Converter with Maximum Power Point Tracking Control*, Master of Science Thesis: KTH Royal Institute of Technology, Stockholm, Sweden.
- Jiang, Y., J. A. A. Qahouq, and T. A. Haskew, 2013, "Adaptive step size with adaptive-perturbation-frequency digital MPPT controller for a single sensor photovoltaic solar system," *IEEE Transactions on Power Electronics*, Vol. 28, No. 7, pp. 3195–3205.
- Kim, H., W. Liu, and Z. Ren, 2015, "Efficiency and output power of thermoelectric module by taking into account corrected Joule and Thomson heat," *Journal of Applied Physics*, Vol. 118, No. 11, p. 115103.
- Kotak, V. C., and P. Tyagi, 2013, "DC To DC Converter in Maximum Power Point Tracker," *Journal of Advanced Research in Electrical, Electronics and Instrumentation Engineering*, Vol. 2, No. 12, December 2013.
- Kumar, S., et al., 2013, "Thermoelectric Generators for Automotive Waste Heat Recovery Systems Part I: Numerical Modeling and Baseline Model Analysis," *Journal of Electronic Materials*, Vol. 42, No. 4, pp. 665–674.
- Leonov, V., and P. Fiorini, 2007, "Thermal matching of a thermoelectric energy scavenger with the ambiance," *Proceedings of the European Conference on Thermoelectrics*, pp. 129–133.
- Leyva, R., et al., 2006, "MPPT of photovoltaic systems using extremum-seeking control," *IEEE Transactions on Aerospace and Electronic Systems*, Vol. 42, No. 1, pp. 249–258.
- Li, M., 2011, "Thermoelectric-Generator-Based DC-DC Conversion Network for Automotive Applications," Master of Science Thesis: KTH Royal Institute of Technology, Stockholm, Sweden.

- Lian, K. L., J. H. Jhang, and I. S. Tian, 2014, "A maximum power point tracking method based on perturb-and-observe combined with particle swarm optimization," *IEEE Journal on Photovoltaic*, Vol. 4, No. 2, pp. 626–633.
- Mehta, R.J. ,Y. Zhang, C. Karthik, B. Singh, R. W. Siegel, T. Borca-Tasciuc, and G. Ramanath, 2012, "A new class of doped nanobulk high-figure-of-merit thermoelectrics by scalable bottom-up assembly," *Nature Materials* 1, pp. 233-240.
- Philip, N., et al., 2013, "Investigation of maximum power point tracking for thermoelectric generator," *Journal of Electronic Materials*, Vol. 42, No. 7, pp. 1900–1906.
- Piegari, L. and R. Rizzo, 2010, "Adaptive perturb and observe algorithm for photovoltaic maximum power point tracking," *IET Renewable Power Generation*, Vol. 4, No. 4, pp. 317–328.
- Poudel, B.,Q. Hao, Y. Ma, Y. Lan, A. Minnich, B. Yu, X. Yan, D. Wang, A. Muto, D. Vashaee, X. Chen, J. Liu, M.S. Dresselhaus, G. Chen, and Z.F. Ren, 2008, "High-thermoelectric performance of nanostructured bismuth antimony telluride bulk alloys," *Science* 320, pp. 634-638.
- Yan, X., G. Joshi, W. Liu, Y. Lan, H. Wang, S. Lee, J. Simonson, S. Poon, T. Tritt, G. Chen, and Z.F. Ren, 2012, "Enhanced thermoelectric figure of merit of p-type Half-Heuslers," *Nano Letters*, 11, pp. 556-560.
- Yau, H. T. and C. H. Wu, 2011, "Comparison of extremum-seeking control techniques for maximum power point tracking in photovoltaic systems," *Energies*, Vol. 4, pp. 2180–2195.

Appendix A

Numerical Analysis of Maximum Peak Power with Extremum-Seeking Control

Appendix A

Numerical Analysis of Maximum Peak Power with Extremum-Seeking Control

Numerical analysis of the MPP with ESC is summarized here for the case of a sine wave perturbation. This analysis is adapted from Philip et al. (2013). The nonlinear static map of a TEG is presented as

$$P = f(V) = P_{max} + \frac{P''}{2} (D - D_m)^2 \quad (A1)$$

where D is the duty cycle of the PWM controller and D_m is the value of the unknown optimal duty cycle. The objective is to minimize the quantity $(D - D_m)$ so that the output function, (V) , approaches its maximum value at P_{max} . The estimated value of D_m is denoted as D_{est} . The perturbation signal $B\sin(\omega t)$ is the input that is used for measuring the gradient information of the function $f(V)$. The estimated duty cycle error, denoted as D_e ,

$$D_e = (D_m - D_{est}) \quad (A2)$$

The quantity D_{est} is modulated by a signal $B\sin(\omega t)$ in order to obtain the duty cycle, D . Therefore, Equation (A2) can be expressed as

$$D - D_m = B\sin(\omega t) - D_e \quad (A3)$$

Substitute Equation (A3) into the Equation (A1) to obtain

$$P = f(V) = P_{max} + \frac{P''}{2} (D_e - B\sin(\omega t))^2 \quad (A4)$$

Expanding Equation (A4) and replacing $\sin^2(\omega t)$ with $1/2(1 - \cos^2(\omega t))$ provides

$$P = P_{max} + \frac{P''}{2} B^2 + \frac{P''}{2} D_e^2 - BP''D_e \sin(\omega t) - \frac{P''}{4} B^2 \cos^2(\omega t) \quad (A5)$$

A high-pass filter removes the slow DC component of the power in Equation (A5)

$$\frac{s}{s + \omega_h} P \approx \frac{P''}{2} D_e^2 - BP''D_e \sin(\omega t) - \frac{P''}{4} B^2 \cos^2(\omega t) \quad (A6)$$

Here s is the Laplace variable.

The signal in Equation (A6) is demodulated by multiplying by a dither signal $\sin(\omega t)$, to obtain

$$\xi = \frac{P''}{2} D_e^2 - BP''D_e \sin^2(\omega t) - \frac{P''}{4} B^2 \cos^2(\omega t) \sin(\omega t) \quad (A7)$$

Replacing $\cos^2(\omega t)$ with $\sin^2(\omega t)$, the Equation (A7) becomes

$$\xi = -\frac{BP''}{2} D_e + \frac{BP''}{2} D_e \cos(\omega t) + \frac{B^4 P''}{8} (\sin^3(\omega t) - \sin(\omega t)) + \frac{P''}{2} D_e^2 \sin(\omega t) \quad (A8)$$

The term in *Equation (A8)* is very small and can be neglected. This reduces *Equation (A8)* to

$$\xi = -\frac{BP''}{2}D_e + \frac{BP''}{2}D_e \cos(\omega t) + \frac{B^4P''}{8}(\sin 3(\omega t) - \sin(\omega t)) \quad (\text{A9})$$

The last two terms in *Equation (A9)* are high-frequency signals and are attenuated when passed through an integrator. Thereby reducing *Equation (A9)* to

$$D_{est} = -\frac{k}{s}\left(\frac{BP''}{2}\right)D_e \quad (\text{A10})$$

The derivative is then

$$\dot{D}_{est} = -\left(\frac{kBP''}{2}\right)D_e \quad (\text{A11})$$

Because D_m is constant in *Equation (A2)*, the derivative of *Equation (A2)* is expressed as

$$\dot{D}_e = -D_{est} \quad (\text{A12})$$

Substitute *Equation (A11)* into *Equation (A12)* to obtain

$$\dot{D}_e = -\left(\frac{kBP''}{2}\right)D_e \quad (\text{A13})$$

Because $\frac{kBP''}{2}$ is positive, the system is stable and it can be concluded that as $D_e \rightarrow 0$, D_{est} converges within a small region of D_m , which corresponds to the MPP.